



Tomographic image of the crust and upper mantle beneath the western Tien Shan from the MANAS broadband deployment: Possible evidence for lithospheric delamination

Li Zhiwei ^{a,1}, Steve Roecker ^{a,*}, Li Zihai ^b, Wei Bin ^b, Wang Haitao ^b, Gennady Schelochkov ^c, Vitaly Bragin ^c

^a Rensselaer Polytechnic Institute, Troy, NY, USA

^b Provincial Bureau of Seismology of Xinjiang, Urumqi, China

^c Research Station of the Russian Academy of Sciences, Bishkek, Kyrgyzstan

ARTICLE INFO

Article history:

Received 29 July 2008

Received in revised form 4 March 2009

Accepted 12 May 2009

Available online 20 May 2009

Keywords:

Tien Shan

Tomography

Continental collision

Delamination

Central Asia

ABSTRACT

We combine teleseismic P arrival times from the recent MANAS deployment of broadband sensors with P and S arrival times from local events recorded by the GENGHIS deployment and analog observations from the Kyrgyz Institute of Seismology to generate a high resolution (~20 km) image of elastic wavespeeds in the crust and upper mantle beneath the western Tien Shan. The total data set consists of 29,006 P and 21,491 S arrivals from 2176 local events recorded at 144 stations along with 5202 P arrivals from 263 teleseismic events recorded at 40 stations. The most significant feature in our image of the mantle beneath the Tien Shan is a pair of large, elongated high wavespeed regions dipping in opposite directions from the near surface to depths of at least 400 km. These regions appear to be continuous and extend upwards to bounding range fronts where the Tarim Basin is being overthrust by the Kokshal range on the south side, and the Kazach shield underthrusts the Kyrgyz range on the north side. While it is tempting to interpret these high wavespeed anomalies as evidence for contemporary subduction of continental lithosphere, such a scenario is difficult to reconcile with both the timing of the orogen and the size of the wavespeed anomaly. We suggest instead that they represent downwelling side-limbs of a lithospheric delamination beneath the central part of the Tien Shan, possibly by siphoning of the bordering continental lithosphere as the central part descends.

© 2009 Elsevier B.V. All rights reserved.

1. Introduction

The Tien Shan, the most prominent mountain belt of Central Asia (Fig. 1), is the best example of contemporary intracontinental orogenesis. Spanning some 2500 km in length and attaining a maximum width of ~400 km at its western extent, the Tien Shan is composed of a system of east–west trending ranges and intermontane basins passing through China, Kyrgyzstan, Kazakhstan, Uzbekistan, and Tajikistan. Notable both for some of the highest elevations (>7000 m) outside of the Himalaya–Karakorum belt, and some of the most active seismicity (the only historic great earthquakes in a continental setting), the mountain belt developed largely in response to collision of the Indian subcontinent with the southern margin of Eurasia over the last 50 million years (Molnar and Tapponnier, 1975). The location of this orogen, some 1000–3000 km from the former southern plate boundary of Eurasia (now marked by the Indus–Tsangpo suture), sits within continental crust that originated from the

accretion of numerous Paleozoic terranes in Central Asia (Burtman, 1975; Sengor et al., 1993).

While it is conceptually straightforward to relate the intraplate deformation of the Tien Shan to the Alpine–Himalayan collisional system, it is less clear what factors control the timing and location of this deformation within a much larger region composed of a complex assemblage of geological terranes. Reactivation of old structures in the crust from previous tectonic episodes provides a logical explanation for localization of the deformation. However, some of these old structural features are reactivated while others are not, suggesting that the dynamics of this mountain belt are more likely controlled by recently evolved structures of the crust and mantle. Nevertheless, the roles these structures play in any such localization are largely unresolved.

From 2005 to 2007, participants in the Middle AsiaN Active Source (MANAS) project collected geophysical (magnetotellurics along with active and passive source seismology) observations in order to address a number of questions related to the manner in which deformation is accumulating across the Tien Shan. The main objective of the passive source seismology component of the project was to collect and analyze data from a dense deployment of broadband seismic stations in order to generate an image of the upper mantle. In this paper we describe the first order results obtained from a

* Corresponding author.

E-mail address: roecks@rpi.edu (S. Roecker).

¹ Current address: Key Laboratory of petroleum Resources Research, Institute of Geology and Geophysics, Chinese Academy of Sciences, Beijing, China.

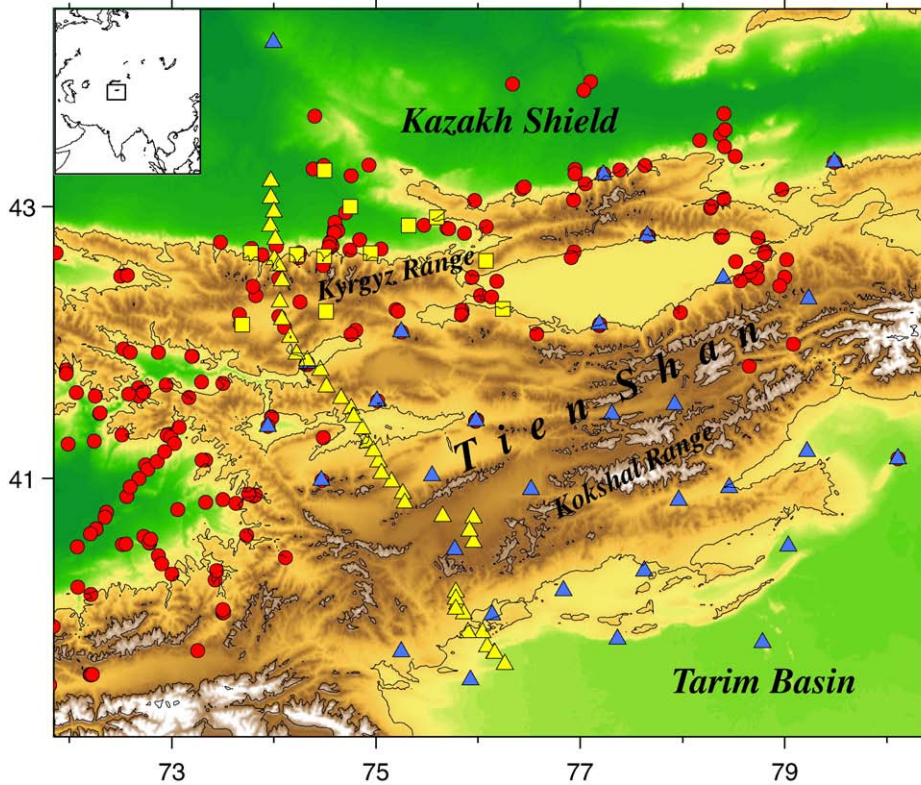


Fig. 1. Topographic map of the western Tien Shan and surrounding regions. Location of map is shown in the inset at the upper left. Symbols locate the seismic stations of the four networks used in this study: Yellow triangles indicate the seismic stations of the MANAS deployment, blue triangles the GHENGIS deployment, yellow squares are KNET, and red circles are the analog stations of the Kyrgyz Institute of Seismology. (For interpretation of the references to color in this figure legend, the reader is referred to the web version of this article.)

tomographic analysis of a selection of teleseismic arrival times recorded by this deployment.

2. Data

The data used in this study comes from four sources: the MANAS, GHENGIS (Roecker, 2000, 2001), and Kyrgyz Network (KNET) broadband digital seismographs and the Kyrgyz Institute of Seismology (KIS) analog network (Fig. 1). The primary data set we use for generating images of the mantle is from MANAS, a quasi-linear deployment of seismographs that operated from June, 2005 until July, 2007. MANAS consisted of 40 broadband sensors, 20 Streckeisen STS-2s and 20 Guralp CMG-3ESPs, deployed along a NNW-SSE profile extending from the Kazach shield in the north to the Tarim Basin in the south. Each three component station recorded continuously at 100 sps using Quanterra Q330 acquisition systems.

For this study we selected a set of 263 teleseismic events (Fig. 2) of magnitude ($M > 5.5$) and distance range ($30^\circ < \Delta < 100^\circ$) suitable for the tomographic algorithm we employ. 5202 P wave arrival times for these events were determined by waveform correlation using a technique similar to that described by VanDecar and Crosson (1990). Uncertainties were assigned based on the correlation coefficient and the size of the time shift on the final iteration. Generally these uncertainty estimates are on the order of 0.1 s.

We use local event data recorded by the GHENGIS deployment of broadband sensors (Fig. 1) and by the KIS analog network. The entire local data set consists of 29,006 P and 21,491 S arrivals from 2176 local events recorded at 144 stations between 1997 and 2002.

3. Methodology

The arrival time tomography techniques we employ in this study are similar to those described in Roecker et al. (2004, 2006), the

principle difference being that we adopt a spherical rather than Cartesian coordinate system to accommodate the much larger area under investigation. Because some of the ray paths we analyze

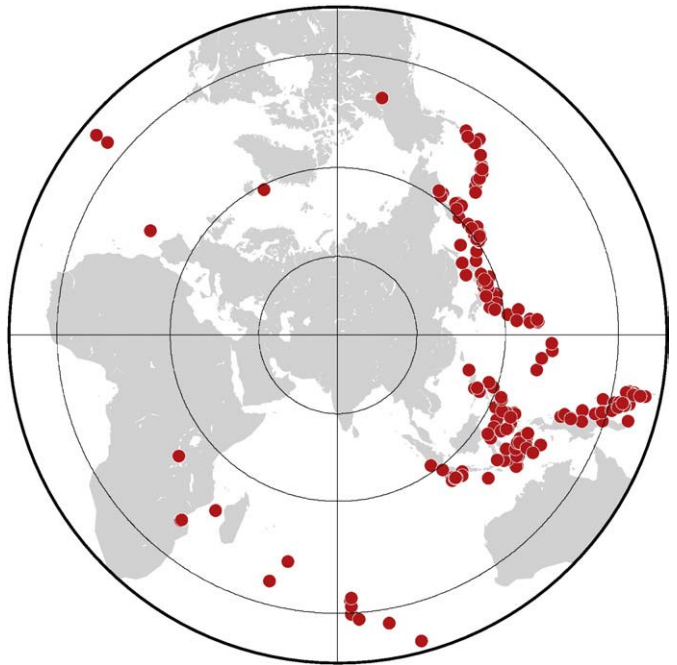


Fig. 2. Map of teleseismic events used to generate the MANAS arrival time data set, plotted as red circles on an azimuthal equidistant projection centered on the Tien Shan. Concentric circles are plotted in increments of 3000 km from the center. Note the predominance of events to the east of the network. (For interpretation of the references to color in this figure legend, the reader is referred to the web version of this article.)

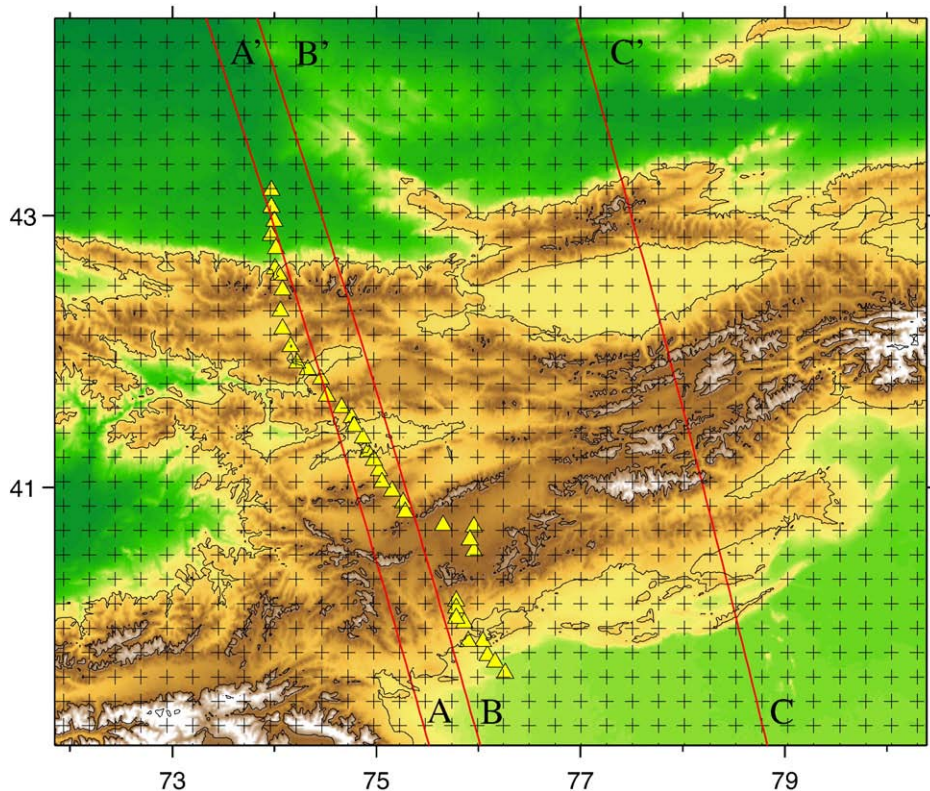


Fig. 3. Grid and cross sections used in the inversion of arrival times for wavespeeds. Yellow triangles locate the MANAS stations for reference. Black crosses locate grid points used to specify wavespeeds for tomography. Red lines denoted by AA', BB' and CC' locate the upper and lower limits of the inclined sections shown in Fig. 7. (For interpretation of the references to color in this figure legend, the reader is referred to the web version of this article.)

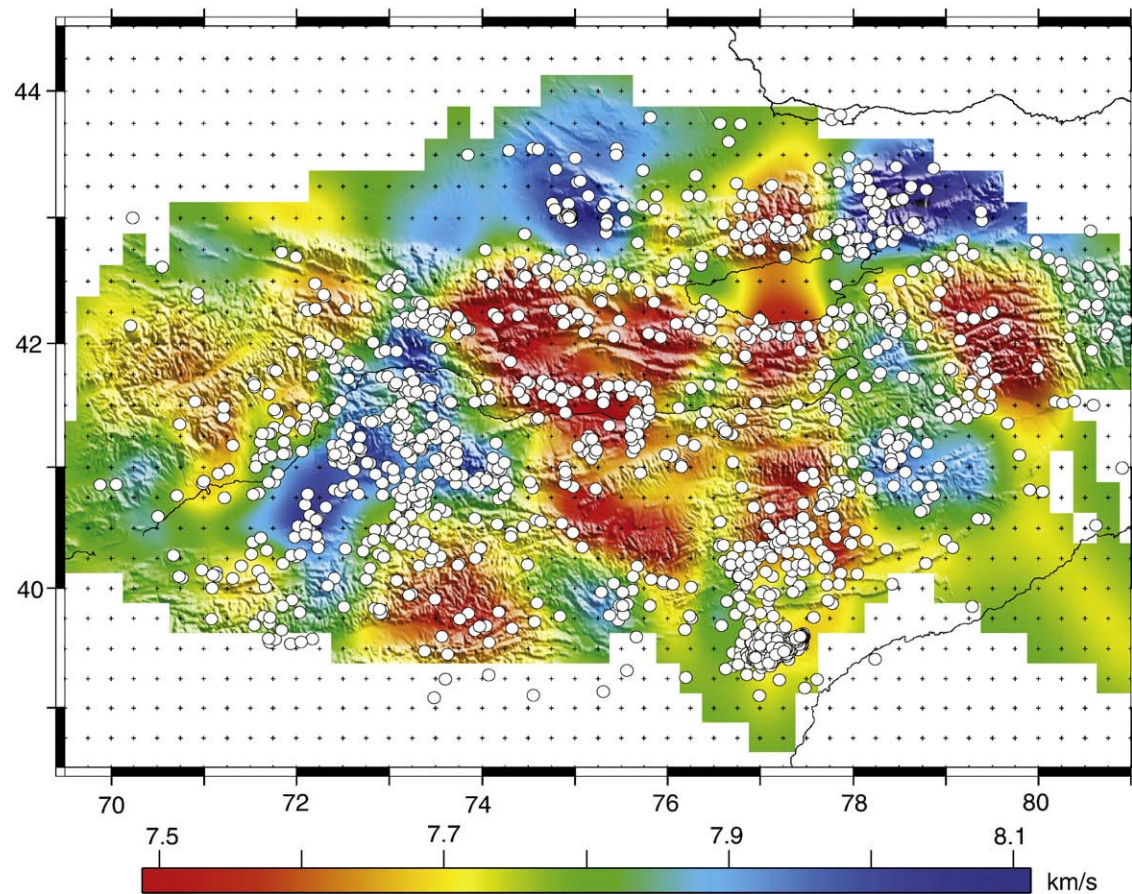


Fig. 4. Map view of P wavespeeds in the uppermost mantle (60 km depth) from an inversion of regionally recorded P and S waves plotted on top of a shaded topographic relief map. Grid point locations are indicated by small crosses. Open circles locate the earthquakes used in the inversion.

travel large distances (>1000 km) laterally through the model the curvature of the Earth needs to be accounted for in some manner. Earth flattening transforms offer a means one way of doing this, but as they specifically apply to great circle paths they are not convenient to a fixed grid system such as we apply here. Hence, we take sphericity directly into account and specify a model of the crust and upper mantle in the region of the Tien Shan by assigning wavespeeds to a mesh of grid points regularly spaced in geocentric latitude, longitude, and depth (Fig. 3). Travel times for rays within the model are computed using an algorithm that adapts the finite difference eikonal equation solver of Hole and Zelt (1995) to a spherical coordinate system. That is, we construct stencils to numerically solve

$$\left(\frac{\partial t}{\partial r}\right)^2 + \left(\frac{1}{r} \frac{\partial t}{\partial \theta}\right)^2 + \left(\frac{1}{r \sin \theta} \frac{\partial t}{\partial \phi}\right)^2 = s^2$$

where t is travel time, s is slowness, θ and ϕ are geocentric colatitude and longitude, respectively, and r is the distance from the center of the Earth. Travel time tables for all points in the mesh are constructed for each receiver in the data set. Initial values of travel times at grid points surrounding the starting point are determined using a “cascading” technique in which a small-scale mesh is used in the vicinity of the point and times are calculated in progressively coarser meshes until the dimensions of the global mesh are reached. Because wavespeeds will be nearly constant in the small-scale mesh, this approach reduces numerical noise in models with significant wavespeed gradients in the vicinity of the starting point.

Teleseismic travel times are determined by combining the times from a given station to the base of the model calculated using the eikonal equation solver with times from the hypocenter to the base using tables generated in a standard Earth model (in this case IASP91; Kennett and Engdahl, 1991). The true travel time is taken from Fermat's principle to be associated with the basal point where the sum of these two contributions is a minimum.

The inverse problem is linearized by Taylor expansion and partial derivatives for each observation are calculated by accumulating contributions along the associated ray path. Perturbations to the wavespeeds in the model are then determined by iteratively solving the resulting system of linear equations using the LSQR algorithm (Paige and Saunders, 1982). A damper of 500 was added used in LSQR to regularize the inversion. This value was chosen by trial and error as a minimum required to produce reasonable perturbations at any iteration. To further mitigate introduction of artifacts, the resulting “raw” perturbations are smoothed using a moving average window that summed over adjacent nodes in all directions before applying them to the model.

Local event data is used at every step of the inversion, either on its own at the outset to generate a starting model for the crust and uppermost mantle or simultaneously with the teleseismic data. Hypocenters of local events are determined by grid search and refined to a subgrid level by interpolation. When incorporating observations from local events, the hypocenter derivatives are added to the general system of equations prior to inversion in order to reduce possible bias towards the prevailing model as discussed, for example, in Roecker et al. (2006). At the same time, we relocate local events at every iteration rather than apply the change in hypocenter estimated in the joint inversion.

In this particular application we choose a fine grid spacing of 5 km for computation of travel times and a nominal coarser grid of 20 km laterally and 50 km in depth for wavespeed inversion (the difference between lateral and vertical spacing reflects anticipated levels of resolution in these directions). The bounds of the model are chosen to include as much useful data as possible as well as enclose regions where heterogeneity is most likely to affect travel time computation. In this case we extend our model from 60 km depth to an elevation

above the highest station (stations are embedded into the model so that differences in elevation can be explicitly accounted for).

4. Results

To reduce the influence of heterogeneity in the crust on inferred mantle wavespeeds, and to generate a starting model consistent with the mesh we use to parameterize the Earth, we began our analysis by determining a model for the crust and uppermost mantle using local events recorded by the GHENIS and KIS networks (Fig. 4). Although we use more data and have better coverage than the studies of Xu et al. (2006, 2007), ours is a fairly coarse scale model and we do not discuss the details here, other than to point out that it does not differ qualitatively from those previous models. The main purpose of this model is to provide reasonable travel time corrections through this very heterogeneous part of the medium.

In imaging the upper mantle beneath the Tien Shan, we initially attempted an inversion of a combination of teleseismic arrival times from all four sources of data (MANAS, KIS, GHENGIS, and KNET). This approach proved to be unsuccessful, however. The images produced were less coherent and noticeably dependant on the particular subset of data used. Moreover, the reduction in residual variance for the GHENGIS and KIS data sets was only on the order of a few percent. We suspect that the quality of the arrivals in the GHENGIS and KIS data sets is uneven, a hypothesis borne out by an abundance of unreasonably large residuals associated with arrivals reported to be of good quality (Fig. 5). We are aware that the GHENGIS data set is contaminated by clock errors that are difficult to quantify, and the KIS data suffers from the usual ailments of analog seismograms. While it

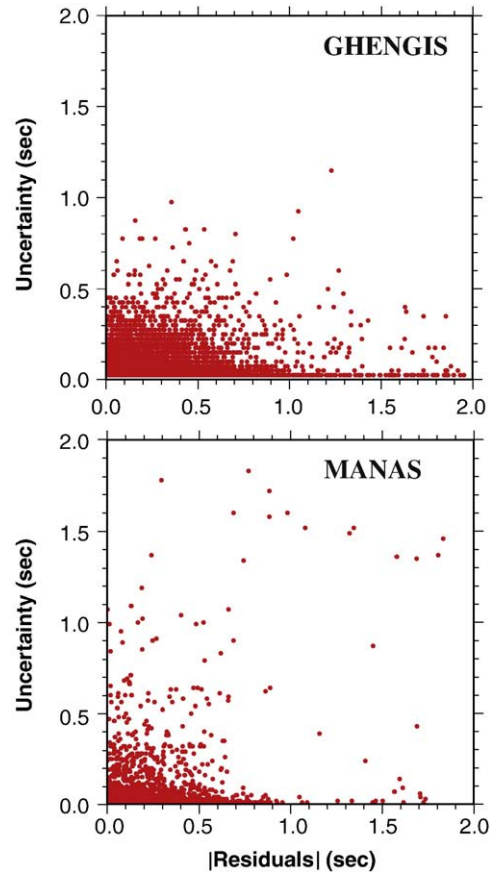


Fig. 5. Plots of picking uncertainties vs absolute values of travel time residuals for teleseismic arrivals from the GHENGIS (upper) and MANAS (lower) data sets. The large number of arrivals with residuals much greater than the quoted uncertainty in the GHENGIS data set leads us to suspect that it is contaminated by outliers.

should be possible to glean some useful information from these data sets, for example by the exclusion of suspect data using a priori estimates of quality (Pavlis, personal communication, 2002), the more uniform quality of the MANAS and KNET data sets persuaded us to focus solely on arrival times from these networks for purposes of this study.

While restricting the sources of data improves data quality, the linear geometry of the MANAS array combined with a predominance of earthquake locations to the east reduces spatial sampling. Ray paths to the MANAS network traverse a limited band within the mantle (Fig. 6), hence even though we perform a full three-dimensional inversion of the data, the image we produce will be essentially two dimensional. Therefore, we examine the results of our modeling where the wavespeeds are best resolved by passing a plane through the Earth from the surface to the bottom of the model in the region of highest ray density and restricting our attention to the wavespeeds determined in and near this plane (located by lines AA'–CC' in Fig. 3).

Our preferred model was obtained after three iterations. The a posteriori residual standard deviation is 0.22 s, a 50% reduction from that of the starting model (a combination of the crustal model obtained from local events and the 1D model obtained by Roecker et al., 1993) but still somewhat higher than the anticipated noise level of 0.1 s shown in cross section (upper left of Fig. 7), the outstanding features of this model are two relatively high wavespeed slabs extending from close to the surface to depths in excess of 400 km. The

two slabs appear to be about 100 km thick and dip towards each other. A projection of the northern slab to the surface aligns approximately with the Krygyz range front, while that from the southern body aligns with the boundary between the Kokshal range and the Tarim Basin. We also note that the uppermost mantle located directly beneath the main part of the Tien Shan at depths between about 100 km and 200 km between the high wavespeed slabs is a region of low wavespeeds (~2–3% lower than the background).

While our preferred projection coincides with maximum ray density, we also plot our results in alternate sections to demonstrate the extent to which our interpretation may be biased by a particular choice of orientation. The first (upper right of Fig. 7) is a dipping section slightly offset NW of optimal; while the coherence of the primary features degrades somewhat they are nevertheless still clearly seen. The other two projections (lower row of Fig. 7) are standard vertical sections. The slabs show up in these sections in those areas where they are likely to be well resolved, and of course disappear where there is no data.

4.1. Resolution tests

As with any tomographic image, it is necessary to establish the degree to which important features are robust and which are likely to be artifacts created by the particular geometry of the data set. In addressing this question we take the usual approach of imaging test

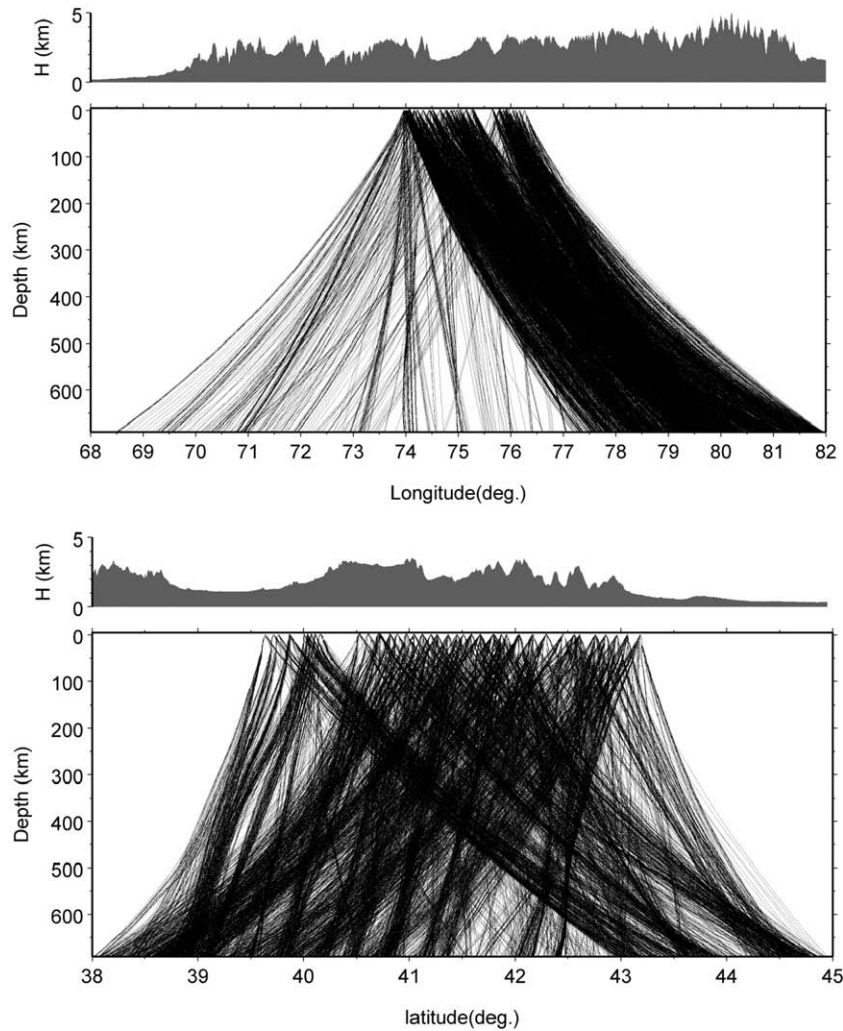


Fig. 6. Ray paths for all the teleseismic arrival times used in the inversion, plotted as a function of longitude (upper) and latitude (lower). Note the predominance of rays arriving from the east. We select a region of maximum resolution based on the density of ray paths to generate the slanted cross section shown in Fig. 7.

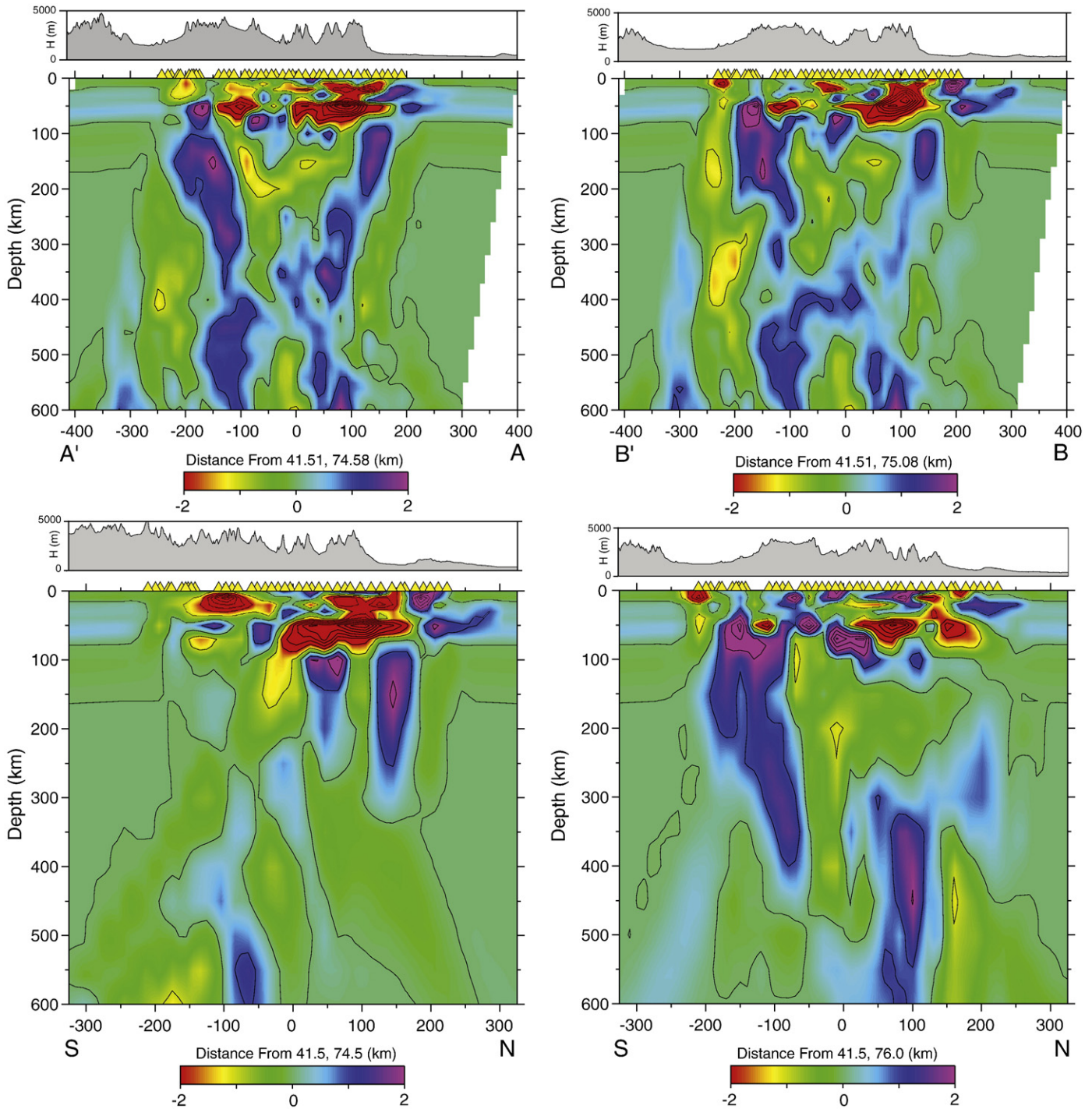
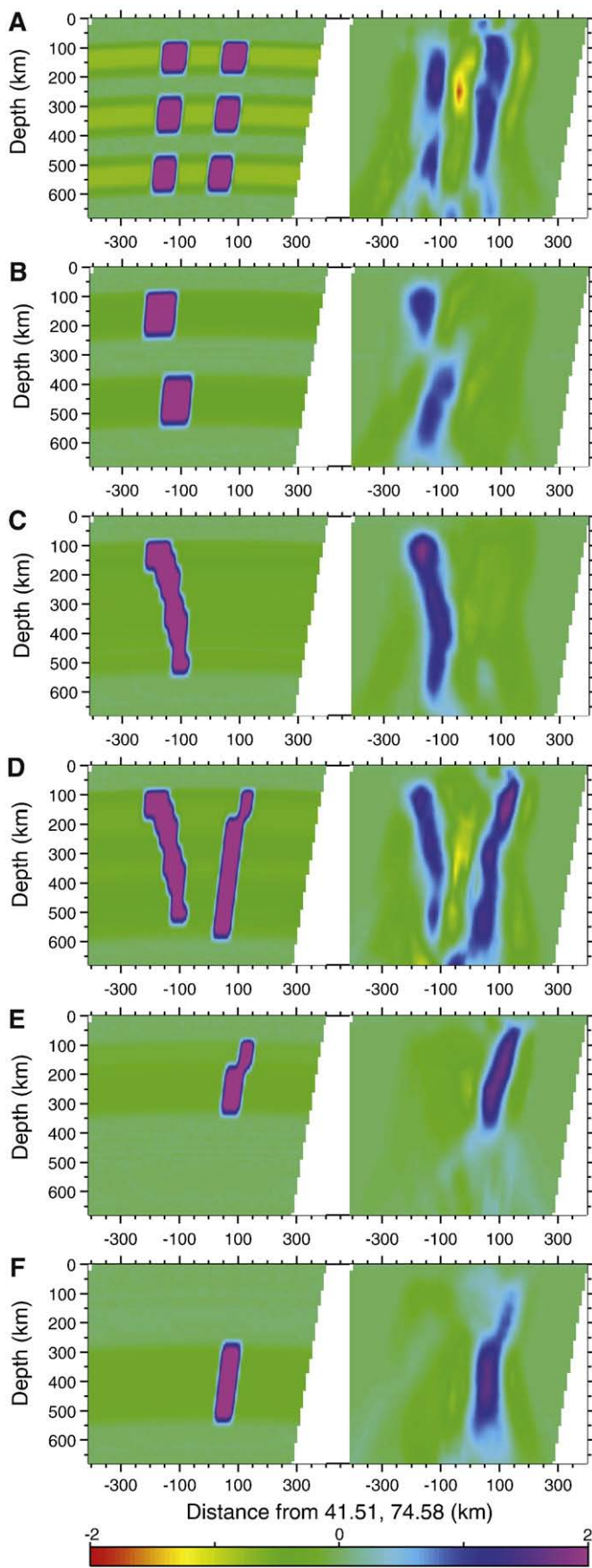


Fig. 7. Perturbations to P wavespeed (dV_p/V_p) from an average 1D background model determined by inversion of the teleseismic travel time residuals. The locations of the slanted cross sections are shown in Fig. 3; the maximum resolution projection onto a plane extending from AA' to CC' is shown on the upper left. A slightly displaced plane from BB' to CC' is shown on the upper right. The vertical axis in these sections is true depth in km (as opposed to down-dip length). The lower two plots are NS sections taken at 74.5° (left) and 76.0° (right) longitude. The 74.5° section has better resolution at shallow depths in the north, while the 76.0° section has better resolution at shallow depth in the south. Perturbations relative to the 1D average background wavespeeds are in percent as indicated in the palettes below each section. Locations of the MANAS stations are shown as yellow triangles at the surface. Topography along each section is shown in the box above each section. (For interpretation of the references to color in this figure legend, the reader is referred to the web version of this article.)

data sets, but instead of performing standard checkerboard tests we tailor these data sets to address specific questions about the principle features we observe in our image. For example, because the most important feature in our image is the steeply dipping high wavespeed slabs, an obvious question is to what extent these structures are created by smearing of a smaller anomaly along near-vertical teleseismic ray paths. We show here the results of six such tests

(Fig. 8). The first (Row A in Fig. 8) consists of a series of discrete high wavespeed blocks in the vicinity of the high wavespeed slabs and is intended to be a straightforward test of spatial resolution. The recovered image shows that, as may be expected, while lateral resolution is quite good, it is difficult at this spacing and orientation to distinguish between discrete blocks and continuous slabs. At the same time, the second test (Row B in Fig. 8) shows that if discontinuous



features are offset laterally they can be distinguished from one another. Hence, as long as these structures are not vertically dipping we should be able to say if deeper bodies are attached to the shallower ones. The third and fourth tests (Rows C and D in Fig. 8) show the degree to which a large, continuous high wavespeed body can smear to deeper depths. Again, while the lateral dimension of the body is well resolved, there is a tendency to smear vertically. The final two tests (Rows E and F in Fig. 8) demonstrate the degree to which high wavespeeds associated with the northern slab can be resolved. These tests demonstrate that, while some vertical smearing is evident, the entire high wavespeed zone is not likely created by a single deep or shallow anomaly.

Comparing the results of these tests to our image of the upper mantle, we conclude from the excellent lateral resolution afforded by this data set that these two high wavespeed bodies are distinct from one another, and that, because neither of these features are vertical in the upper 400 km, they most likely are continuous from the near surface down to at least that depth. Below 400 km depth these high wavespeed zones become approximately vertical, and hence could be an artifact caused by smearing of shallower anomalies. Hence, while these features may extend below 400 km depth, we have less confidence in their existence at these depths.

5. Discussion

The unusual nature of the mantle beneath the western Tien Shan has been documented by several previous seismological studies, starting with Vinnik and Saipbekova (1984) who inferred a low wavespeed upper mantle from averages of teleseismic residuals. Their inference was corroborated by a tomographic image produced by Roecker et al. (1993) and a receiver function study by Kosarev et al. (1993) who suggested that the Kyrgyz Tien Shan is underlain by a hot, rising asthenosphere that provides isostatic support for elevated topography. Anomalous SKS splitting directions reported by Makeyeva et al. (1992) also were interpreted as strike-parallel flow of the asthenosphere related to siphoning of the lithosphere beneath the Tien Shan. Based on delay times of Ps converted phases that showed a 20 km elevation of the 410-km discontinuity beneath the range, Chen et al. (1997) suggested that the Tien Shan may represent an area of active lithospheric delamination. A study of S receiver functions (Oreshin et al., 2002) suggested that the region of very low velocity in the upper mantle determined by Roecker et al. (1993) begins at a depth of about 90 km, and moreover that trends in teleseismic P and S wave residuals are consistent with the presence of melt in this low velocity region. The mantle flow directions determined by Makeyeva et al. (1992) and Wolfe and Vernon (1998) from SKS splitting were revisited by Vinnik et al. (2002a,b), who combined SKS with the transverse component of P receiver functions to determine the depth dependence of anisotropy. They found that SKS splitting is mainly due to anisotropy at depths greater than about 100 km (i.e., where Oreshin et al. (2002) determined low shear wavespeeds).

More recent tomographic work by Yang (2003) and Yang et al. (2003; hereafter Y03) and Lei and Zhao (2007; hereafter LZ07) also show low wavespeeds in the uppermost mantle beneath the western

Fig. 8. Cross sections of resolution tests. The left column shows the true wavespeed model for each test; in each case the blue anomaly is two-dimensional (extending in and out of the poster) and represents a 2% increase over the background wavespeed. The right column shows reconstructions taken along the same AA'-CC' slanted cross section used in the upper left of Fig. 7. (A) Test of vertical resolution showing that some geometries can be completely smeared by the inversion, although (B) shows that north dipping segmented bodies can be resolved. (C) and (F) show that long continuous features can be smeared to deeper depths, meaning that we can not resolve the depth extent below depths of about 400 km. (D) shows that the two slabs can be resolved laterally, and (E) shows that if the Kazach body were shallow it would not appear to extend artificially to great depth. (For interpretation of the references to color in this figure legend, the reader is referred to the web version of this article.)

Tien Shan, but additionally show evidence for high wavespeed, slab like structures in the upper mantle. Both of the above studies image a north dipping, high wavespeed slab associated regionally with the Tarim Basin. However, while the Y03 image shows a slab extending nearly to the surface, LZ07 suggest that it is detached and somehow suspended or slowly sinking into the upper mantle while being replaced by upwelling asthenosphere. Both studies also find a high wavespeed anomaly associated with the Kazakh shield, but this part of the Y03 image was poorly resolved while LZ07 claim that this high wavespeed anomaly is restricted to depths less than 150 km. LZ07 interpret the deeper, north dipping slab to be a detached piece of subducted lithosphere from the south (i.e., associated with the Tarim Basin) while the northern anomaly is associated with contemporary underthrusting of the Kazakh shield.

The image we generated in the present study shows the same low wavespeeds in the uppermost mantle suggested by nearly all prior studies in the other. As Y03 and LZ07, we also image high wavespeed bodies in the upper mantle associated with both the Tarim Basin and the Kazakh shield, but the specifics of these bodies are significantly different from either of the previous studies. First, the body we associate with the Tarim Basin is in approximately the same location as that reported by Y03, but is located somewhat to the south of that found by LZ07 and is continuous up to shallow depths. Second, our image suggests that the south dipping body associated with the Kazakh shield is not restricted to shallow depths as in LZ07 but instead reaches depths as great as 400 km.

The existence of any high wavespeed body in the upper mantle beneath the Tien Shan not directly related to lithospheric thickening is difficult to explain as there is no evidence for oceanic subduction since the Paleozoic. Any relic subduction would have to remain suspended in the mantle and at the convergent boundary of an ongoing collision for 100's of millions of years. This would require the slabs to remain attached in situ to the continental lithosphere for a very long period of time, and also displace the mantle ahead of them as shortening progressed. While individual slabs conceivably can retreat as they sink under their own weight or migrate under and orogen and they are overthrust by an overriding plate, it is difficult to imagine how two negatively buoyant slabs could push forward in opposite directions through the mantle.

Subduction of a large amount of continental lithosphere is difficult to reconcile with the very recent (<15 Mya) history of convergence in the area deduced from the current high rate of shortening across the entire range (presently about 22 mm/yr; Abdurakhmatov et al., 1996; Reigber et al., 2001) and the modest amount of total shortening (~80 km) estimated from the crustal budget (Roecker, 2001; Thompson et al., 2002). Even if a significant amount of continental crust were dragged into the mantle and left out of the total shortening (and there is no evidence from the tomography that this has happened), there does not seem to be nearly enough time to subduct lithosphere from both sides of the range to 400 km depth. An additional issue is the relatively small wavespeed anomaly represented by these slabs; they appear in Y03, LZ07, and in this study to be on the order of 2–3% higher than the surrounding mantle, which is much smaller than one would anticipate for a contrast between recently subducted continental lithosphere and asthenosphere. For example, Oreshin et al. (2002) report wavespeed contrasts at the lithosphere–asthenosphere boundary in this region of ~7–8% from receiver function studies. For all these reasons we view a subduction related interpretation of these high wavespeed bodies to be unlikely.

We suggest instead that, following a model examined by Houseman et al. (1981), that these high wavespeed bodies represent limbs of lithosphere that have been siphoned deep into the mantle as the lithosphere in the central part of the western Tien Shan delaminated. A freefalling, detached lithospheric root could potentially sink very quickly into the mantle, so that a detachment 15 my ago could easily have sunk to depths as great as 400 km and displace the 410 km

discontinuity as reported by Chen et al. (1997). The low amplitude wavespeed anomaly, presumably caused by a temperature contrast with the surrounding mantle, could be explained through conservation of heat as the surrounding lithosphere is elongated to greater depths. If the delamination event took place too quickly and recently for conduction to heat the lithosphere, and presuming a constant specific heat and dV_p/dT , then reducing the wavespeed contrast by, for example, a factor of four would involve decreasing the temperature contrast by a similar factor. This in turn would mean that the original heat content of the lithosphere is distributed over a volume about 4 times greater than the original. In other words, this thermal anomaly is what one would roughly expect from stretching a 100 km thick lithosphere to 400 km.

6. Conclusions

Combining arrival time observations from a variety of sources, we constructed an image of the elastic wavespeeds in the crust and upper mantle beneath the central Tien Shan. Our image of the uppermost mantle beneath the central part of the range is consistent with those determined in previous studies, and confirms that there is at present only a thin (less than about 100 km depth) lithospheric lid beneath the central part of the belt. Both of the range fronts are associated with large, slab like regions with wavespeeds 2–3% higher than those of the ambient mantle. Resolution tests suggest that these regions extend from the surface to at least 400 km depth, and perhaps deeper. An interpretation of these features consistent with what we know about the evolution and kinematics of the mountain belt is that these features are related to the decent of a recently delaminated lithosphere from the central part of the belt. Such a scenario would allow these features to develop despite the short history of rapid convergence across the belt. A recent delamination would also explain why convergence across the belt accelerated in the last 10–15 my as deformation resistant lithosphere was replaced by more compliant asthenosphere.

Acknowledgements

Many people were responsible for the collection and initial processing of the data we analyzed in this study. In particular we would like to thank Wei Ruoping of PBSX (Urumqi), Liu Qiyuan of the Chinese Earthquake Administration (Beijing) and Sasha Matix of RS RAS (Bishkek) for their help with logistics. Albina Adamova (KIS in Bishkek) helped us with the KIS analog data and also helped create the correlated travel time data set. We benefited from discussions with Peter Molnar, who suggested the delamination scenario to us as an explanation for the high wavespeed anomalies. We also benefited from comments from Gary Pavlis and an anonymous reviewer. All of the broadband seismic equipment used in the MANAS and GHENGIS projects was provided by the IRIS PASSCAL program. This work was supported by the NSF Continental Dynamics Program (EAR-0309927).

References

- Abdrakhmatov, K. Ye, et al., 1996. Relatively recent construction of the Tien Shan inferred from GPS measurements of present-day crustal deformation rates. *Nature* 384, 450–453.
- Burtman, V.S., 1975. Structural geology of the Variscan Tien Shan. *Am. J. Sci.* 275A, 157–186.
- Chen, S.W., Roecker, Y.H., Kosarev, G.L., 1997. Elevation of the 410-km discontinuity beneath the central Tien Shan: evidence for a detached lithospheric root. *Geophys. Res. Lett.* 24, 1531–1534.
- Hole, J.A., Zelt, B.C., 1995. 3-D finite-difference reflection traveltimes. *Geophys. J. Int.* 121 (2), 427–434.
- Houseman, G., McKenzie, D.P., Molnar, P., 1981. Convective instability of a thickened boundary layer and its relevance for the thermal evolution of continental convergent belts. *J. Geophys. Res.* 86, 6115–6132.
- Kennett, B.L.N., Engdahl, E.R., 1991. Traveltimes for global earthquake location and phase identification. *Geophys. J. Int.* 105, 429–465.

- Kosarev, G.L., Petersen, N.V., Vinnik, L.P., Roecker, S.W., 1993. Receiver functions for the Tien Shan analog broadband network: contrasts in the evolution of structures across the Talasso–Fergana fault. *J. Geophys. Res.* 98, 4437–4448.
- Lei, J., Zhao, D., 2007. Teleseismic P-wave tomography and the upper mantle structure of the central Tien Shan orogenic belt. *Phys. Earth Planet. Inter.* 162, 165–185.
- Makeyeva, L.I., Vinnik, L.P., Roecker, S.W., 1992. Shear-wave splitting and small-scale convection in the continental upper mantle. *Nature* 358, 144–147.
- Molnar, P., Tapponnier, P., 1975. Cenozoic tectonics of Asia; effects of a continental collision. *Science* 189, 419–426.
- Oreshin, S., Vinnik, L.P., Peregovodov, D., Roecker, S., 2002. Lithosphere and asthenosphere of the Tien Shan imaged by S receiver functions. *Geophys. Res. Lett.* 29 (8), 1191.
- Paige, C.C., Saunders, M.A., 1982. LSQR: an algorithm for sparse linear equations and sparse least squares. *TOMS* 8 (1), 43–71.
- Reigber, C., Michel, G.W., Galas, R., Angermann, D., Klotz, J., Chen, J.Y., Papschev, A., Arslanov, R., Tzurkow, V.E., Ishanov, M.C., 2001. New space geodetic constraints on the distribution of deformation in Central Asia. *Earth Planet. Sci. Lett.* 191, 157–165.
- Roecker, S., 2000. Crustal thickness and mantle anisotropy of the western Tien Shan from the analysis of GHENGIS broadband seismic data. *EOS Trans. Suppl.* 81.
- Roecker, S., 2001. Constraints on the crust and upper mantle of the Kyrgyz Tien Shan from the preliminary analysis of GHENGIS broadband data. *Russ. Geol. Geophys.* 42, 1554–1565.
- Roecker, S.W., et al., 1993. Three-dimensional elastic wave velocity structure of the western and central Tien Shan. *J. Geophys. Res.* 98, 15779–15795.
- Roecker, S., Thurber, C., McPhee, D., 2004. Joint inversion of gravity and arrival time data from Parkfield: new constraints on structure and hypocenter locations near the SAFOD drill site. *Geophys. Res. Lett.* 31, L12 S04. doi:[10.1029/2003GL019396](https://doi.org/10.1029/2003GL019396).
- Roecker, S., Thurber, C., Roberts, K., et al., 2006. Refining the image of the San Andreas Fault near Parkfield, California using a finite difference travel time computation technique. *Tectonophysics* 426, 189–205.
- Sengor, A.M.C., Natal'in, B.A., Burtman, V.S., 1993. Evolution of the Altaiid tectonic collage and Paleozoic crustal growth in Eurasia. *Nature* 364, 299–307.
- Thompson, S.C., Weldon, R.J., Rubin, C.M., Abdurakhmatov, K., Molnar, P., Berger, G.W., 2002. Late Quaternary slip rates across the central Tien Shan, Kyrgyzstan, central Asia. *J. Geophys. Res.* 107 (B9), 2203.
- VanDecar, J.C., Crosson, R.S., 1990. Determination of teleseismic relative phase arrival times using multi-channel cross-correlation and least squares. *Bull. Seismol. Soc. Am.* 80, 150–169.
- Vinnik, L.P., Saipbekova, A.M., 1984. Structure of the lithosphere and the asthenosphere of the Tien Shan. *Ann. Geophys.* 2, 621–626.
- Vinnik, L.P., Peregovodov, D., Makeyeva, L., Oreshin, S., Roecker, S., 2002a. Towards 3-D fabric in the continental lithosphere and asthenosphere: the Tien Shan. *Geophys. Res. Lett.* doi:[10.1029/2001GL014588](https://doi.org/10.1029/2001GL014588).
- Vinnik, L.P., Roecker, S., Kosarev, G.L., Oreshin, S.I., Koulakov, I.Yu., 2002b. Crustal structure and dynamics of the Tien Shan. *Geophys. Res. Lett.* 29 (22), 2047.
- Wolfe, C.J., Vernon, F.L., 1998. Shear-wave splitting at central Tien Shan: evidence for rapid variation of anisotropic patterns. *Geophys. Res. Lett.* 25, 1217–1220.
- Xu, Y., Roecker, S.W., Wei, R., Zhang, W., Wei, B., 2006. Analysis of seismic activity in the crust from earthquake relocation in the central Tien Shan. *Bull. Seismol. Soc. Am.* 96, 737–744.
- Xu, Y., Li, Z., Roecker, S.W., 2007. Uppermost mantle structure and its relation with seismic activity in the central Tien Shan. *Geophys. Res. Lett.* 34, L10304. doi:[10.1029/2007GL029708](https://doi.org/10.1029/2007GL029708).
- Yang, X., Teleseismic Tomography of the Tien Shan, M.S. thesis, Indiana University, 129 p., 2003.
- Yang, X., Pavlis, G.L., Roecker, S.W., Vernon, F.L., 2003. Teleseismic tomographic images of the central Tien Shan. *EOS-Trans. AGU* 84, 1057.